Powder Technology 394 (2021) 214–224

Contents lists available at ScienceDirect

Powder Technology

journal homepage: www.elsevier.com/locate/powtec

Anisotropic particle synthesis and characterization for lithium-ion battery electrode materials via precursor precipitate growth inhibitor

Chen Cai, Hongxu Dong, Gary M. Koenig Jr *

Department of Chemical Engineering, University of Virginia, 102 Engineers Way, Charlottesville 22904-4741, VA, USA

ARTICLE INFO

Article history:
Received 5 June 2021
Received in revised form 12 August 2021
Accepted 16 August 2021
Available online 18 August 2021

Keywords:
Particle morphology
Lithium-ion battery
Anisotropy
Coprecipitation

ABSTRACT

To achieve higher power and energy density batteries, electrodes are often designed towards increased current densities and thicknesses. Under such conditions, electrode microstructure can become an important factor. Electrode microstructure is dependent on many factors, but one factor that can facilitate anisotropic microstructures is having anisotropic lithium-ion battery active material particles. Thus, robust methods to produce active materials with anisotropic particle morphologies are desirable. This manuscript will describe the use of an inhibitor to direct anisotropic morphologies of lithium-ion battery precursor particles. This anisotropic secondary platelet morphology was retained after conversion to final active material particles. The synthesis method should be generally applicable to producing a variety of transition metal oxide compositions with anisotropic morphologies, however, the inhibitor can have significant impacts on the rate of precipitation of the transition metals during precursor synthesis. Three exemplar materials will be described towards targeted synthesis of anisotropic cathode particles.

1. Introduction

The increasing power demands of portable electronics, the need for high performance energy storage for electric vehicles, and the desire for low cost and reliable large-scale energy storage systems for utilities have motivated the development of new battery materials and technologies [1]. Desired attributes for these batteries include high energy density, high power density, and long cycle life [1–4]. Due to advantages especially with regards to those attributes, lithium-ion (Li-ion) batteries have been the dominant technology in recent deployments for the applications above. Due to its relative contribution to the weight and cost of Li-ion battery cells, cathode materials and electrodes have received significant attention [5–7]. Much research in improving Li-ion battery performance with regards to the electroactive materials in the cathode has been in the materials chemistry, which includes both new chemistry and crystal structures (e.g., layered $LiCoO_2$, olivine $LiFePO_4$, and spinel $LiMn_2O_4$) and modifications in the composition of the electroactive materials (e.g., layered $LiNi_{0.8}Mn_{0.1}Co_{0.1}O_2$) [8,9].

In addition to the exploration of new materials chemistry, composition, and phase, modification and control over the microstructure of battery electrodes also can improve the energy and power density of battery cells [10–14]. In particular, alignment of the pore microstructures within Li-ion electrodes in the direction of Li^+ flux reduces the tortuosity in the electrode microstructure, improving effective transport properties and reducing concentration polarization in the cell [11,12,15]. Aligned pores in the electrode microstructure can be achieved using a variety of methods, including using external applied fields to create aligned voids during electrode processing and using etching processes after fabricating electrodes to induce vertical channels [16]. Another strategy to template anisotropic microstructures and aligned pores is to start with anisotropic electroactive particles and align the particles within the electrodes. In an example of using this strategy, Billaud et al. successfully aligned graphite flakes in an electrode with the goal of improving Li^+ transport [16]. This report demonstrated increased capacity at high charge/discharge rates with the aligned particle/pore electrodes. As a key first step in applying this strategy there must be an anisotropic morphology of the secondary particles of the electroactive materials. Thus, the goal in this manuscript will be to produce anisotropic electrode active material particles using a robust synthesis approach.

The synthesis approach used in this study to produce anisotropic secondary battery active material particles was coprecipitation of precursors with defined morphologies followed by calcination to final materials. Coprecipitation has been previously demonstrated as a method to synthesize precursors for multicomponent transition metal (TM) oxides. Coprecipitation has the advantages of lab accessibility, scalability, morphology tunability [17–24], and mixing homogeneity of multiple TM components throughout the secondary particles [25–27]. Precursor particle morphologies can be adjusted by tuning the reaction conditions, and subsequently these morphologies have been demonstrated

* Corresponding author at: Department of Chemical Engineering, University of Virginia, 102 Engineers' Way, P.O. Box 400741, Charlottesville, VA 22904, USA.
E-mail address: gary.koenig@virginia.edu (G.M. Koenig).

https://doi.org/10.1016/j.powtec.2021.08.060
0032-5910/

to be well-retained after the calcination process to produce final active materials [28,29]. For this report, the coprecipitation anion chosen was oxalate ($C_2O_4^{2-}$). Oxalate has advantages relative to choosing other systems such as carbonate and hydroxide in that most oxalate processes are stable in air atmosphere and the phase purity of the crystals formed is high for a wide range of compositions, particularly for compositions using popular battery TMs Mn, Co, and Ni [21,30–36]. Additionally, oxalate ions in the solution play a dual role as both a precipitation reagent and a complexing agent [37–39]. The formation of metal complexes with oxalate ions as the ligand slows down the precipitation rate and makes the nucleation and growth processes for the particles more controllable. According to previous reports, oxalate coprecipitation can be used to synthesize precursor particles of narrow size distribution, and particle morphologies were successfully tuned by careful control over solution conditions [30,40].

In this work, oxalate coprecipitation was used to produce anisotropic precipitate particles containing single or multiple TMs. The precipitates were then used as precursor templates to produce Li-ion battery active material particles with anisotropic morphologies. To demonstrate the generality of this approach, electrode materials of $LiMn_2O_4$ (LMO) [41], $Li_4Mn_5O_{12}$ [42], and $LiMn_{1.5}Ni_{0.5}O_4$ (LMNO) [43] with anisotropic platelet particles of the desired phase and composition will be reported. However, the techniques for particle synthesis reported herein are not limited to manganese-based materials and should be translatable to produce a variety of anisotropic multicomponent TM oxides. In this manuscript, the precursor and electroactive final materials will be characterized and considerations in their synthesis will be discussed.

2. Experimental

2.1. Transition metal oxalate dihydrate coprecipitation synthesis

Oxalate precipitate particles containing TM of either pure Mn or Mn/Ni blends were synthesized using an adapted procedure from previous reports [44]. 100 mM of sodium oxalate ($Na_2C_2O_4$, Fisher Chemical) was dissolved in 400 mL of deionized (DI) water and heated to 60 °C. In some cases, 10 mM of sodium citrate dihydrate ($Na_3C_6O_7H_5{\bullet}2H_2O$, Sigma-Aldrich) was added to the dissolved $Na_2C_2O_4$ solution. Separately, 100 mM of soluble TM were dissolved in another 400 mL of DI water. The soluble TM composition was either 100% of manganese sulfate monohydrate ($MnSO_4{\bullet}H_2O$, Fisher Chemical) or 81.7% of $MnSO_4{\bullet}H_2O$ / 18.3% of nickel sulfate hexahydrate ($NiSO_4{\bullet}6H_2O$, Fisher Chemical). The two solutions were then combined all at once (thus having 5 mM citrate during the reaction for cases where citrate was added) and allowed 30 min reaction time with 300 RPM stirring at 60 °C. The precipitate was collected via vacuum filtration followed by rinsing of the filter cake with 1.6 L DI water. The resulting powder was then dried at 80 °C overnight in air atmosphere.

The resulting powders were TM oxalate dihydrates [44,45]. For the Mn/Ni blend precursor, note that the target was an overall total 3:1 Mn:Ni stoichiometry in the precipitate particles. As will be discussed in further detail later, an excess of Mn in the solution feed was necessary to achieve this stoichiometry in the resulting particles precipitated in the presence of the citrate additive.

2.2. Tracking of transition metal concentration during synthesis

For some experiments, the soluble concentration of each TM (Ni, Mn) was monitored as a function of time during the coprecipitation reaction using a method previously reported [44]. To determine the soluble TM concentration as a function of time, 1 mL of solution was drawn and filtered by 200 nm syringe filter at time points of 1, 2, 3, 5, 10, 15, 20, 25, and 30 min after initiation of the coprecipitation reaction. The total volume of the reactor was 800 mL, and thus the sum of the volumes of the samples drawn was less than 1.5% of the total reactor solution and was not expected to have a significant impact on the mixing profile or total reagent available in the reactor. After forcing the drawn liquid from the reactor through the filter, the solutions which passed through were then added to a 27.75 vol% hydrochloric acid (Sigma-Aldrich) / 9.25 vol% nitric acid (Macron) aqueous solution to eliminate the possibility of precipitate formation in the filtered solution. The TM ion concentrations were then measured by ICP-OES (PerkinElmer Optima 8000). Solutions evaluated using ICP-OES had been diluted to concentrations of a few ppm of the TMs.

2.3. Electrode material synthesis

Precursor produced via coprecipitation, $MnC_2O_4{\bullet}2H_2O$ and $Mn_{0.75}Ni_{0.25}C_2O_4{\bullet}2H_2O$ (relative TM composition in the solid confirmed via ICP), were blended with Li_2CO_3 (Fisher Chemical) at 5% extra stoichiometry of added Li. Blending was done by hand using mortar and pestle for 10 min. The mixed powder was then transferred into the furnace (Carbolite CWF 1300) and fired in an atmosphere of ambient lab air. For LMO, the temperature profile was 700 °C for 20 h. For $Li_4Mn_5O_{12}$, the temperature profile was 500 °C for 72 h. For LMNO, the temperature profile was at 800 °C for 6 h followed by a hold at 700 °C for 10 h. The heating rate to reach the hold temperature for all cases was 1 °C min^{-1}, and the cooling rate back to ambient temperature was not controlled.

2.4. Material characterization

Scanning electron micrographs (SEM) and energy dispersive x-ray spectroscopy (EDS) was conducted on powders using a FEI Quantum 650. Powder x-ray diffraction (XRD) patterns for materials were collected using a PANalytical X'pert ProMPD. Tap density was measured using a tap density analyzer (AUTOTAP, Quantachrome Instruments) by tapping 1000 times and then averaging 3 independent measurements. Brunauer–Emmett–Teller (BET) surface area was determined from N_2 adsorption isotherms collected using a NOVA 2200e Surface Area & Pore Size Analyzer (Quantachrome).

2.5. Electrochemical characterization

The electrode materials were mixed with acetylene black (Alfa Aesar) and polyvinylidene difluoride (PVDF, Alfa Aesar) into a slurry using *N*-methyl-2-pyrrolidone as a solvent with a weight ratio of 8:1:1 active material:PVDF:acetylene black. The slurry was blended in a mixer (Thinky AR-100) and then coated onto an aluminum foil using a doctor blade with 200 μm gap size. The coated film was then dried in air overnight at 80 °C, followed by vacuum drying at 80 °C for 3 h. Cathodes used in electrochemical cells were punched from the composite coated on the aluminum foil and a circular punch was used that resulted in a geometric area of 1.33 cm^2.

The cathode was paired with a Li foil anode of an area of 1.6 cm^2, and the electrodes were kept apart using Celgard 2325 separator. The electrolyte used was 1.2 M $LiPF_6$ in 3:7 ethylene carbonate:ethyl methyl carbonate (BASF). A coin cell (CR2032-type) was then fabricated in a glove box filled with argon (<1 ppm H_2O and O_2) and evaluated electrochemically using a multichannel battery cycler (MACCOR). Charge/discharge rates used were determined in advance using C rates based on the mass of cathode in the cells, where 1C was assumed to correspond to 148 mA g^{-1} LMO, 163 mA g^{-1} $Li_4Mn_5O_{12}$, and 147 mA g^{-1} LMNO. The electrode active material loadings were approximately 2.5 mg cm^{-2} for LMO, 2.4 mg cm^{-2} for $Li_4Mn_5O_{12}$, and 4.5 mg cm^{-2} for LMNO. The voltage windows used were 3.5 V to 4.3 V (vs. Li/Li^+) for LMO, 1.9 V to 3.5 V (vs. Li/Li^+) for $Li_4Mn_5O_{12}$, and 3.5 V to 4.9 V (vs. Li/Li^+) for LMNO. Cyclic Voltammetry (CV) experiments with the same voltage range as those used for galvanostatic charge/discharge cycle tests were performed using a Biologic SP-50.

3. Results and discussions

One method to direct precipitate particles towards anisotropic morphologies is to incorporate additives during the coprecipitation reaction which inhibit particle growth by selective binding to crystal facets [46–48]. Of particular relevance to this study, works from Farmanesh et al. have shown that the addition of inhibitors can direct anisotropic particle growth during the precipitation of calcium oxalate monohydrate (COM) [46]. Originating from both electrostatic and stereochemical effects, the citrate ion, which is non-planar and has three carboxylic groups, preferentially docks onto the (100) facet of the COM because of the alignment of the oxalate molecules. Mimicking the oxalate anions, the citrate ions with carboxylic groups binding to the calcium bridge could impede other oxalate ions depositing onto this plane [46,49–51]. While the precipitate in the referenced study was not the same composition as the work presented here, the phase of the resulting particles was still monoclinic structured with same chain arrangement of divalent cations and oxalate anions [52–54]. Thus, it was hypothesized that such inhibitor molecules, in particular citrate, would also slow the growth of Mn or Mn/Ni blend oxalate precipitates and result in anisotropic particles through similar inhibition processes via mimicking the oxalate anion.

3.1. Single electrode materials (LMO and $Li_4Mn_5O_{12}$) with anisotropic morphology characterization

Fig. 1a,b shows the SEM images of pure manganese oxalate dihydrate synthesized in the presence of 5 mM citrate inhibitor during the precipitation reaction. The oxalate particles were highly anisotropic, with long dimensions of ~25 μm and thickness dimensions of ~0.7 μm (Fig. 1a,b). It is noted that the citrate-free $MnC_2O_4{\bullet}2H_2O$ also had a plate morphology, although the length to thickness ratio was much less (for SEM of these materials see the Supporting Information, Fig. S1). Powder XRD patterns can be found in Supporting Information, Fig. S2. XRD patterns were consistent with the presence of only the $MnC_2O_4 \cdot 2H_2O$ without impurity phases [44,55]. The material forms a *C2/c* phase.

The morphology of the corresponding electrode materials (LMO and $Li_4Mn_5O_{12}$) synthesized using the Mn oxalate precursor can be found in Fig. 1c–f. After lithiation, the secondary platelet morphology of the precursor was maintained, although there was increased internal porosity of the particles for both LMO (Fig. 1c,d) and $Li_4Mn_5O_{12}$ (Fig. 1e,f) due to the oxalate decomposition and loss of water from the solid precursor particle structure [30,33,44]. The tap densities of LMO and $Li_4Mn_5O_{12}$ were 0.81 ± 0.02 g cm^{-3} and 0.95 ± 0.02 g cm^{-3} (standard deviations of three independent measurements). The BET surface area for LMO and $Li_4Mn_5O_{12}$ were calculated from N_2 adsorption isotherms (Fig. S3a,b) to be 5.3 m^2 g^{-1} and 20.5 m^2 g^{-1}.

For LMO, the resulting powder XRD pattern was consistent with prior reports for a *Fd-3 m* phase material without any impurity phase (Fig. S4) [56]. However, it is noted that for $Li_4Mn_5O_{12}$ the main peaks were consistent with prior literature reports of the formation of a *Fd-3 m* phase, although a small impurity peak was noted at ~33°, which was attributed to Mn_2O_3 (Fig. S4) [57,58]. The $Li_4Mn_5O_{12}$ also had broader peaks than the LMO material, suggesting relatively lower crystal grain size and/or the presence of lower crystallinity and/or defects in the material.

3.2. Anisotropic morphology controlled multicomponent TM ($LiMn_{1.5}Ni_{0.5}O_4$) electrode material

Fig. 2 displays SEMs of oxalate precipitates containing Ni and Mn, where the reaction conditions were identical except for the absence (Fig. 2a) or presence (Fig. 2b) of 5 mM of added citrate during the synthesis. The molar feed ratio of both oxalate:citrate and TM:citrate was 20:1. Precipitate particles formed in the absence of citrate (Fig. 2a) had an octahedral morphology, while precipitates formed with citrate present (Fig. 2b) had a platelet morphology. These plates were highly anisotropic, with thicknesses of ~0.5 μm and widths of ~10 μm. While the particles in Fig. 2 were all collected after 30 min, it is noted that particles collected during the synthesis containing citrate at 5, 15, and 30 min after initiating precipitation all had platelet morphologies, suggesting that the platelet structure was directed through selective growth of the precipitates form the early stages of the reaction (SEMs of these particles can be found in the Supporting Information, Fig. S5). The width of the platelet particles increased as a function of time, from 5.05 ± 0.80 μm at 5 min to 7.26 ± 0.87 μm at 10 min (uncertainties are standard deviations based on a minimum of 30 independent particle measurements). This significant increase in the width as a function of time suggested that the crystal growth was mainly in the radial direction, which resulted in the anisotropic platelet morphology (measured widths from SEM images as a function of reaction time can be found in Supporting Information, Fig. S6). The results above, when combined, suggested that the citrate inhibited the growth of the Mn and Ni oxalates, and that the inhibition selectively guided the growth of the particles in the radial direction resulting in anisotropic platelet particles.

3.3. Composition of precipitates during coprecipitation reaction

Previous studies have shown that the TM composition of precipitates can significantly deviate from the feed, in particular in low concentration regimes [44]. Compositional deviations can be due to different solubilities for different TMs and/or different rates of coprecipitation [44]. Thus, experiments were performed to track the concentration of each TM as a function of time during the coprecipitation reaction for the case where both Mn and Ni were present to provide insights into the expected compositional homogeneity of the resulting particles. These experiments were performed both in the presence and absence of sodium citrate inhibitor that was found to direct the particles into an anisotropic platelet morphology (Fig. 2) to provide insights into whether the inhibitor had selective impacts on the rate of precipitation of the individual TMs. As mentioned in the Experimental section, the dissolved Mn:Ni ratio in the feed to the coprecipitation reaction was 4.475:1. This ratio was used because it resulted in particles with the desired total Mn:Ni 3:1 ratio for the coprecipitation process with inhibitor included after 30 min of reaction.

When the coprecipitation reaction was performed without inhibitor present, the soluble concentration of both Mn and Ni was measured to drop very quickly (Fig. 3a). Greater than 90% of the Mn and Ni had precipitated within 3 min of initiation of the coprecipitation reaction (Fig. 3b). At early times during the reaction, the Mn and Ni precipitated with the same stoichiometry as the feed solution. However, at later times there was a plateau in the extent of precipitation, and the extent of precipitation of the Ni was greater than the Mn. The greater precipitation of Ni oxalate at longer times was consistent with the lower solubility of Ni oxalate relative to Mn oxalate [44]. In addition, the observation of precipitation at the feed stoichiometry during early times of the reaction was consistent with previous measurements of TM oxalate precipitation [44]. Even if the TM oxalates have different precipitation rates in isolation, seed particles of the faster forming precipitate can facilitate accelerating the precipitation rate of the slower forming precipitate.

The addition of 5 mM sodium citrate inhibitor resulted in significant changes to the loss of Mn and Ni from the solution phase (Fig. 3c). Both TMs precipitated much slower, confirming that the inhibitor did indeed slow the growth of the Ni and Mn oxalate particles. After 3 min, where >90% of the TMs had precipitated in the absence of inhibitor, only 11% of Mn and 8% of Ni had precipitated (Fig. 3d). At the 30 min time point where particles were collected, the precipitation reaction done in the presence of inhibitor was still slowly proceeding, as opposed to having plateaued in the absence of inhibitor. In addition, while at the earliest times the Ni and Mn precipitated at the same stoichiometry as the TM

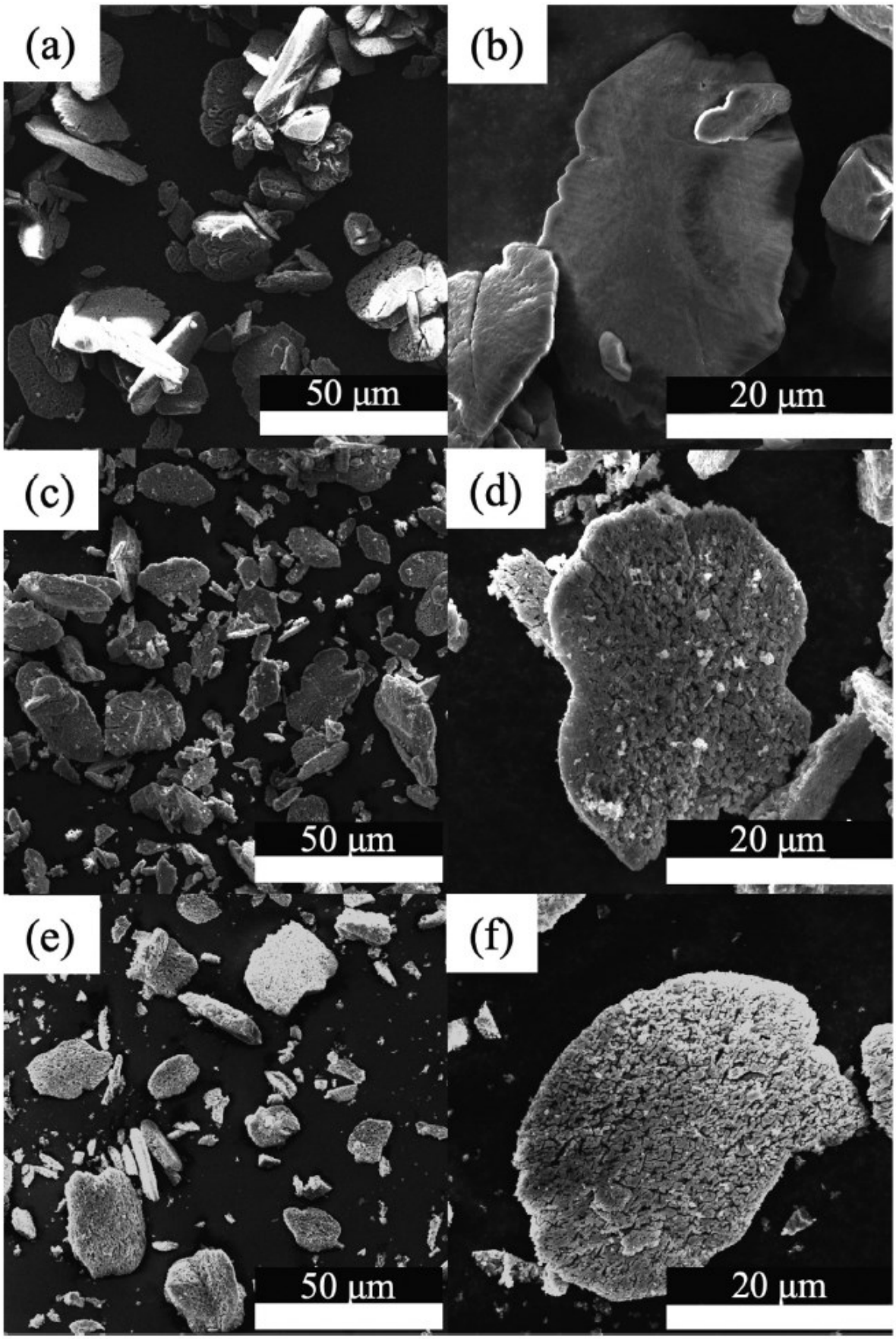

Fig. 1. Scanning electron micrographs of (a, b) $MnC_2O_4{\cdot}2H_2O$, (c, d) LMO, and (e, f) $Li_4Mn_5O_{12}$ at relatively low (a, c, e) and higher (b, d, f) magnification.

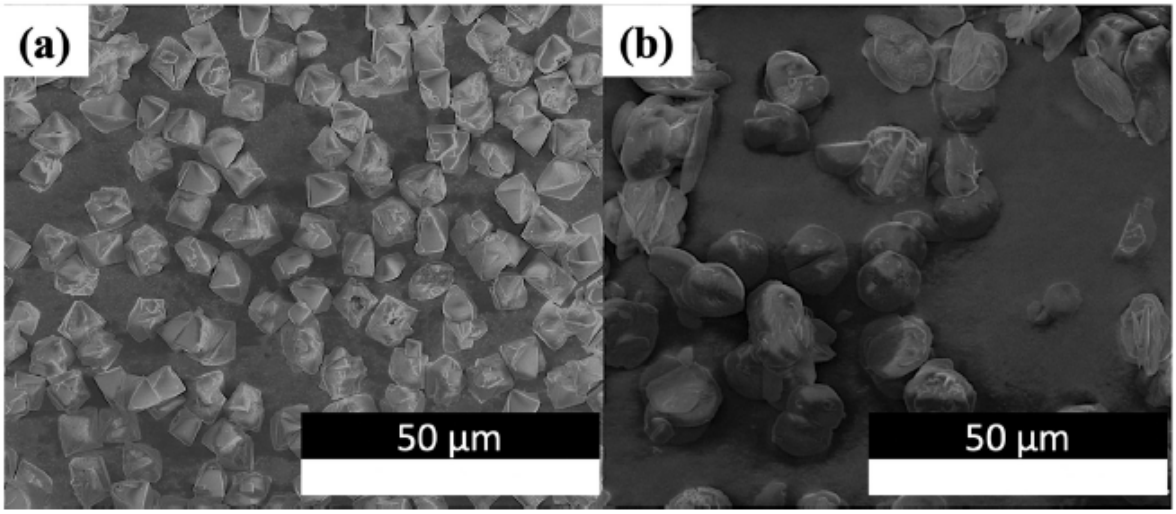

Fig. 2. Scanning electron micrographs of transition metal oxalate precipitate particles (a) without and (b) with the addition of 5 mM sodium citrate inhibitor. Particles were collected 30 min after initiation of the coprecipitation reaction.

feed, starting at ~5 min and later in the process the solid that was deposited was enriched in Ni. The observation that at early reaction times the Mn and Ni precipitated at nearly the feed stoichiometry and that as time proceeded that the composition of the precipitate deposited became increasingly enriched in Ni, coupled with the observation that that the precipitate particles were platelet shaped at very early times and that the plates preferentially grew radially as a function of time (Figs. S5 and S6) suggested that the platelet precipitate particles would have a gradient in composition from Mn-rich towards the center to Ni-rich towards the edge. Further analysis was conducted to confirm whether these TM gradient particles were formed.

The root cause of the increased relative Ni precipitation is an area for future investigation. One possible explanation was the lower intrinsic solubility of Ni oxalate (18 mg kg^{-1} water) than Mn oxalate (310 mg kg^{-1} water) [30,44]. Another possible contributing factor is the ionic radii of the Mn^{2+} (83 pm) and Ni^{2+} (69 pm) in the oxalate lattices [59]. As mentioned earlier in the discussion of Ca oxalate precipitate formation in the presence of citrate, the non-planar citrate ions

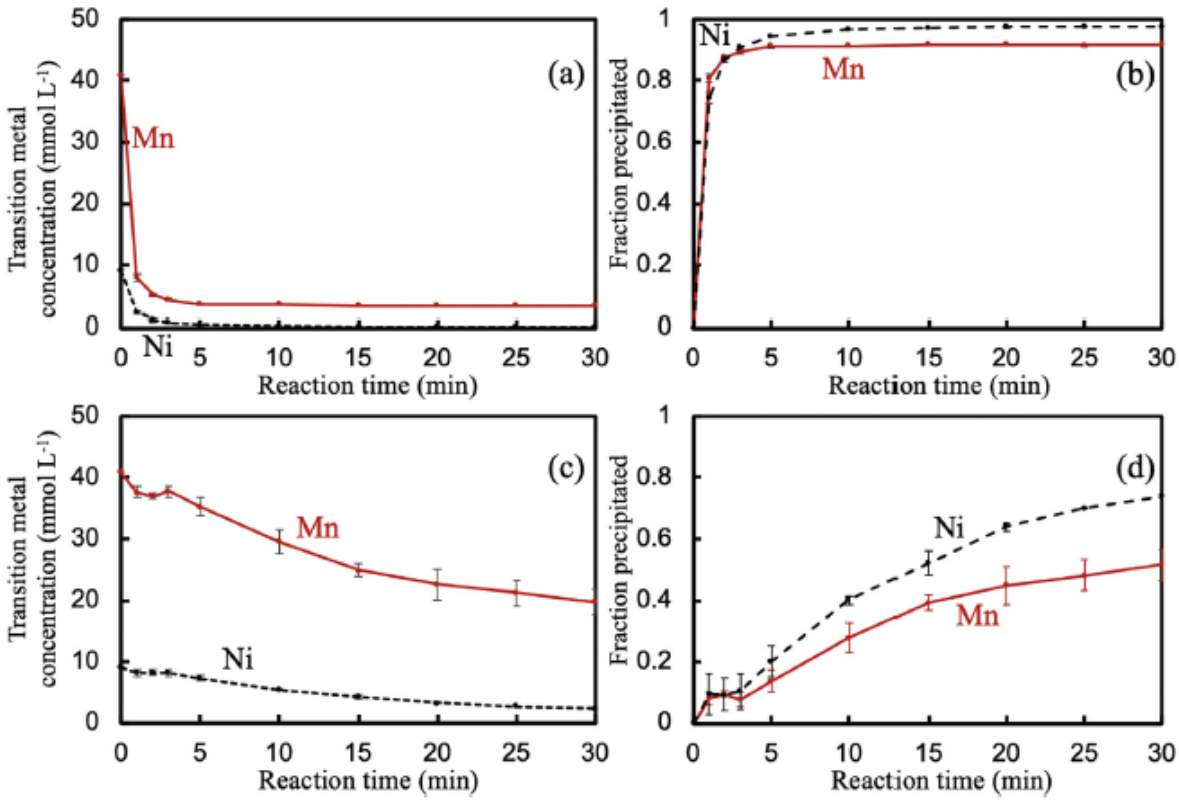

Fig. 3. (a) Soluble Mn and Ni concentration as the coprecipitation reaction with oxalate progressed in the absence of inhibitor. (b) The fraction of the individual Ni and Mn precipitated based on (a). (c) Soluble Mn and Ni concentration as the coprecipitation reaction with oxalate progressed with 5 mM sodium citrate present. (d) The fraction of the individual Ni and Mn precipitated based on (c). For all plots, Mn is solid red lines and Ni is black dashed lines, with the lines added to guide the eye. Error bars are included at the measurement data points and represent the standard deviations of 3 measurements from 3 independent precipitation experiments.

are hypothesized to bind to the TM atoms and mimic the oxalate ions via the enriched carboxylic moieties. The TM atoms aligned in chain arrangement at the oxalate crystal surface with smaller size may impact the citrate binding, for example due to steric effects. Atoms with larger size may not only have modified steric interactions (e.g., more favorable for binding), but also might provide a more favorable surface (slightly larger and/or different surface energy) for binding by the citrate inhibitor. Crystallization growth is a dynamic process of dissolution and deposition, so TM atoms bound by oxalate ions less likely to dissolute back to solution phase than those bound by citrate ions. Thus, it may be that Ni tends to be bound and/or complexed less with citrate ions compared to oxalate ions. In addition, if we examine the nucleation phase in the first 3 min, the precipitation rates for both Mn and Ni were roughly the same, suggesting that in this stage the citrate behaved much less selectively, and the selectivity was more pronounced during later precipitation phases where crystal growth would be expected to play more of a role than initial nucleation with regards to loss of TM from solution [46,49–54]. The detailed solution chemistry is outside the scope of this present work, however, understanding the interactions between the citrate and the crystal and the complexation different TM species in solution would aid in even more explicit control over TM oxalate precipitation processes.

To provide further evidence that the platelet precipitate particles had compositional gradients from the center to the edge of the particle in the radial direction, EDS analysis was conducted on individual particles. First, EDS was averaged over individual platelets that were found lying flat in the SEM on particles collected at different reaction times (Fig. 4a). As the platelet width dimension increased from 5.7 to 10.5 μm, The average Mn:Ni stoichiometry decreased from 3.8:1 to 2.9:1. Note that the Mn:Ni stoichiometry dips below the 3:1 value measured for the final collected particles confirmed by dissolving the particles and conducting ICP. It was suspected this outcome was due to relatively enriched Ni deposition in the slower growing thickness direction of the particles as well. The higher sensitivity of EDS to the surface composition of the material would result in enriched Ni surface also resulting in lower Mn:Ni ratios [60,61]. In any case, the growth of the particles in the radial direction coupled with the decreasing Mn:Ni ratio for the flat presented surface of the particles further supported enrichment in Ni moving from the center to the edge of the plates. In addition, EDS line scans were conducted on individual particles collected at the end of the 30 min of reaction. As shown in Fig. 4b, the relative Mn:Ni was lower towards the edges of the platelet and higher in the center of the platelet, providing further support that these platelet particles had a gradient in TM composition from the center to the edge of the particles. Coprecipitation precursor particles for battery cathode materials have previously been intentionally synthesized to take advantage of different desirable properties of the compositions of the core region compared to the surface [60,62–64]. In these previous reports, the composition gradient was tailored by modifying the dissolved TM feed stoichiometry as a function of time. However, in this present case the gradient resulted from differences in the intrinsic rates of precipitation of the different TM for the solution conditions present. The synthesis strategy reported herein may provide a new route towards TM precursor particles with both compositional gradients and diverse morphologies.

It is noted that while there was a gradient observed in the radial dimension in the Mn and Ni distribution, EDS maps on individual particles suggested that the Mn and Ni were co-located throughout the particles (see Supporting Information, Fig. S7 for a representative EDS map). In addition, the XRD pattern of the $Mn_{0.75}Ni_{0.25}C_2O_4 \cdot 2H_2O$ precipitates did not have any noticeable impurity phases (pattern can be found in Supporting Information, Fig. S2) [53,55]. These results provided evidence that there were not local impurity phases or local grains with deviating Ni and Mn compositions, and that while there was a compositional gradient for the overall particle that at a more local level that the phase and composition was uniform. It is possible that the distribution of Mn and Ni formed a solid solution throughout the precipitate particle.

While the anisotropic platelet precursors with compositional gradients could be beneficial for some materials, the target composition in this study was a 3:1 Mn:Ni ratio throughout the particles to produce the desired LMNO active material. Achieving the 3:1 Mn:Ni target is essential to achieve high electrochemical capacity at high voltage for the LMNO [44,65]. The high voltage capacity in LMNO results from the $Ni^{2+/4+}$ redox couple [44,65]. If the material was enriched in Mn, then the excess Mn would result in $Mn^{3+/4+}$ redox couple participation at a lower voltage than the Ni redox. It is noted that in some cases Mn redox has been reported to be desirable to LMNO due to increased rate capability of the active material [66]. If the active material was enriched in Ni (holding the total TM content constant), the excess Ni increases the likelihood of the formation of rock salt impurity phases, which has previously been demonstrated to degrade electrochemical performance and structural stability of the material with intercalation/deintercalation [67]. Although a gradient in composition was found in

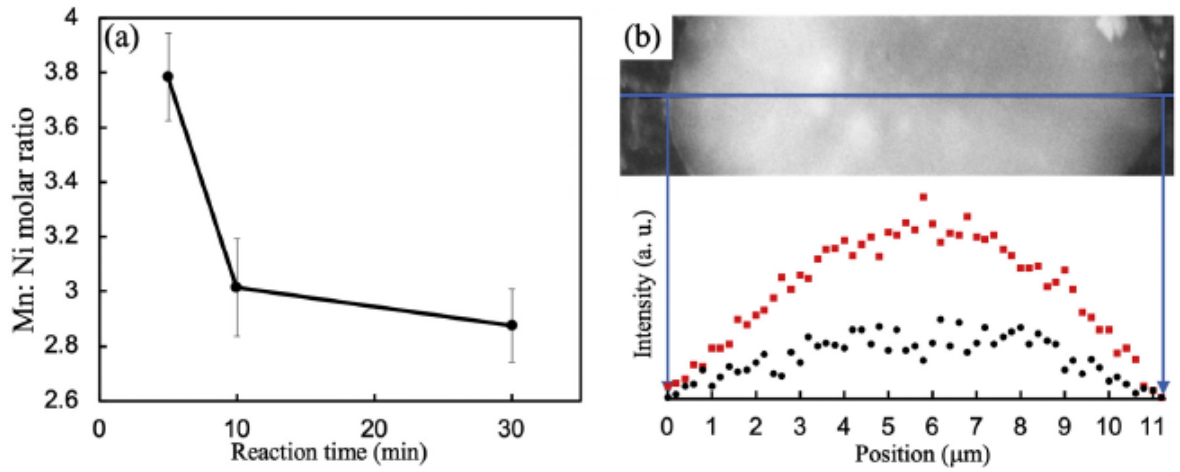

Fig. 4. (a) Average Mn:Ni molar ratio determined from EDS on oxalate particles collected at 5, 10, and 30 min after initiation of the coprecipitation reaction in the presence of inhibitor. EDS was averaged over the area of individual platelet particles which were found lying down flat in SEM images. Error bars represent the standard deviations of a minimum of 3 independent particle measurements. (b) EDS line scan composition for Mn (red squares) and Ni (black circles) on a $Mn_{0.75}Ni_{0.25}C_2O_4 \cdot 2H_2O$ platelet collected at 30 min and precipitated with inhibitor present. The SEM image showing the line scan collection region on the particle analyzed is above the composition data, with arrows pointing to the corresponding positions for the line scan. The total width of the SEM image in (b) is 12 μm.

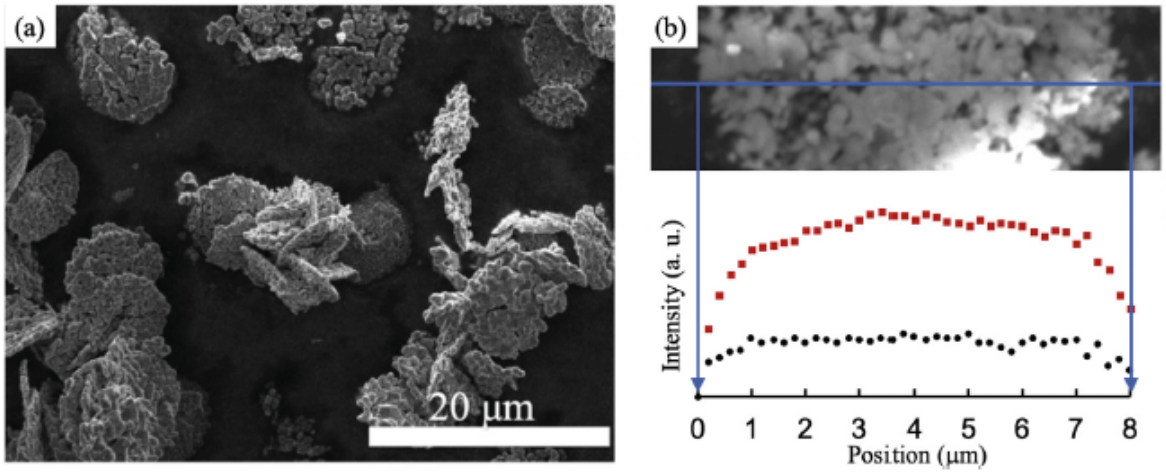

Fig. 5. (a) SEM image of $LiMn_{1.5}Ni_{0.5}O_4$ particles after firing. (b) EDS line scan on $LiMn_{1.5}Ni_{0.5}O_4$ platelet particle with Mn (red squares) and Ni (black circles) composition shown independently. The SEM image showing the line scan collection region on the particle analyzed is above the composition data, with arrows pointing to the corresponding positions for the line scan. The total width of the SEM image in (b) is 10 μm.

the precursor material, the overall total Mn:Ni TM ratio was still 3:1. Thus, when the precursor was blended with a Li source and fired in air, the firing time was chosen to be long enough to facilitate migration of the TM species to achieve homogeneous distribution in the TM oxide active material [27].

After firing and converting the precursor to LMNO active material, the resulting XRD pattern was consistent with reported references (ICDD card No.04–016-3556 [68], the sample and reference XRD pattern can be found in the Supporting Information, Fig. S4). No peaks were observed that suggested the formation of impurity phases, including rock salt impurities [67]. The lattice parameter, assuming the $P4_332$ crystal structure, was calculated to be $a = b = c = 8.1643$ Å and $\alpha = \beta = \gamma = 90°$. The LMNO retained the anisotropic platelet secondary particle morphology of the precursor, although the firing process resulted in internal porosity in the particles (Fig. 5a). This porosity has been previously observed with precipitate precursor particles and oxalates in

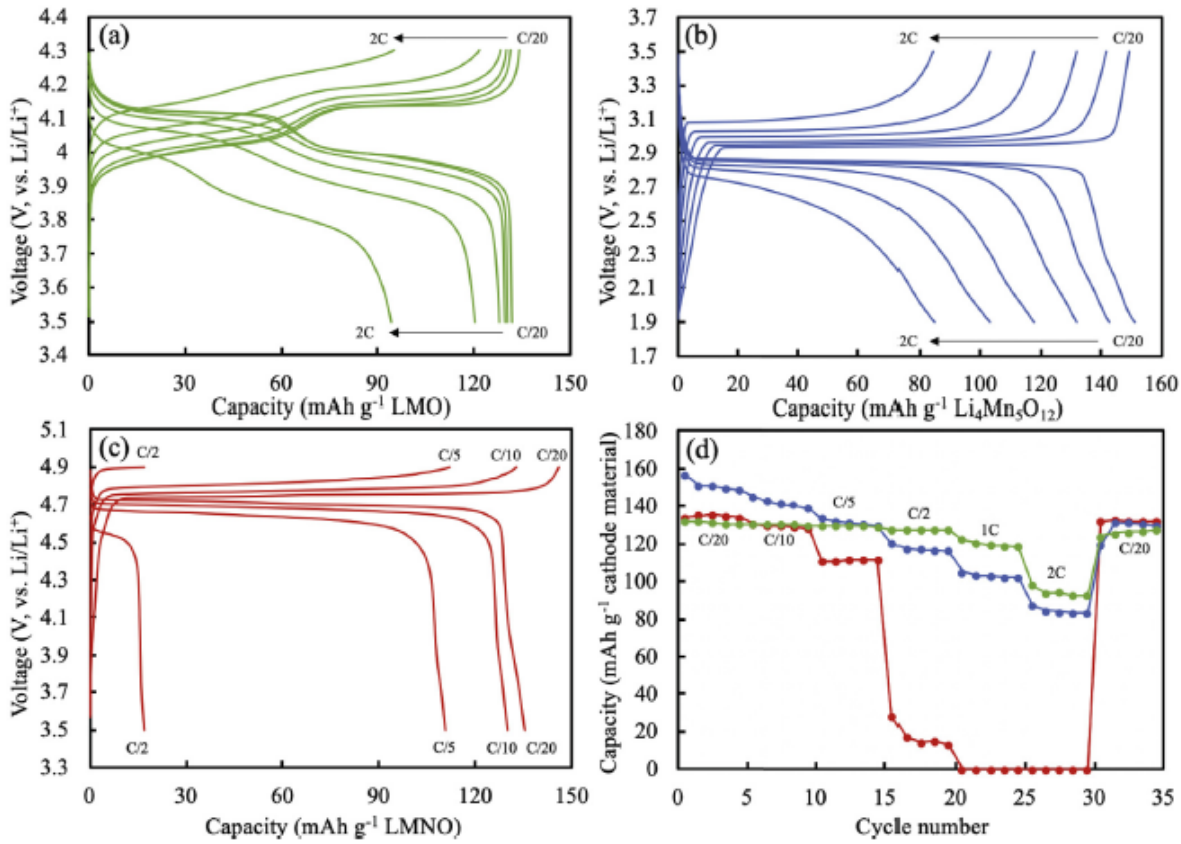

Fig. 6. (a-c) Voltage profiles for cathode materials paired with Li metal anodes, with the curves taken from the second charge/discharge process at each rate (rates used were C/20, C/10, C/5, C/2, 1C, and 2C). The electroactive materials used were (a) LMO, cycled between 3.5 and 4.8 V (vs. Li/Li^+), (b) $Li_4Mn_5O_{12}$, cycled between 1.9 and 3.5 V (vs. Li/Li^+), and (c) LMNO, cycled between 3.5 and 4.9 V (vs. Li/Li^+). Discharge capacity from the rate capability tests for each material can be found in (d) (LMO green, $Li_4Mn_5O_{12}$ blue, and LMNO red). For C rates, 1C corresponded to 0.49 mA (0.36 mA cm^{-2}) for (a), 0.51 mA (0.38 mA cm^{-2}) for (b), and 0.87 mA (0.65 mA cm^{-2}) for (c). Charge and discharge cycles were both conducted at the same noted C rate.

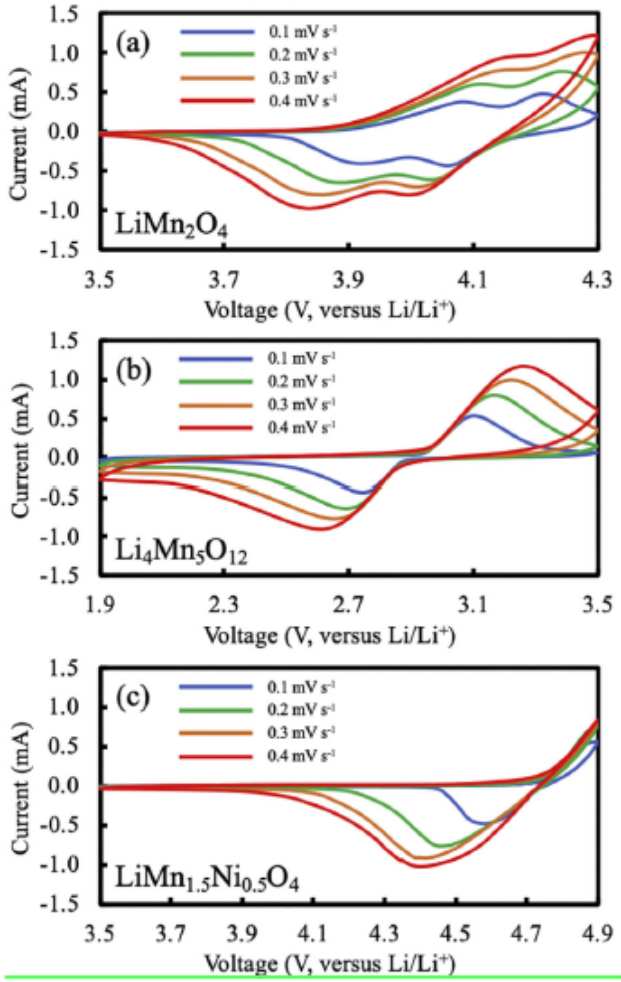

Fig. 7. CV profiles for (a) LMO, (b) $Li_4Mn_5O_{12}$, and (c) LMNO. The blue, green, orange, and red curves represent the scan rates at 0.1 mV s^{-1}, 0.2 mV s^{-1}, 0.3 mV s^{-1}, and 0.4 mV s^{-1}, respectively.

particular [27], and has been attributed to voids formed when the water and oxalate leave the precursor during firing as also mentioned for the LMO and $Li_4Mn_5O_{12}$ materials earlier. The bulk composition of the LMNO was confirmed to have a 3:1 Mn:Ni TM stoichiometry using ICP.

To provide support that the firing conditions homogenized the compositional gradient in the platelet particles, EDS line scans were conducted on particles that were found lying flat in the SEM. As can be seen in a representative example in Fig. 5b, the compositional profile was much more consistent from the core towards the edge compared to the precursor particles (Fig. 4b). The material spent a total of 16 h at temperatures exceeding 700 °C, allowing the gradient in composition to relax and become more homogeneous. It is noted that the edges of the line scan appear to have gradients in composition, although the effects of being near the edge of the particle and having increasing contributions from the background substrate in the SEM make it difficult to conclude that there was a gradient remaining in these regions. The tap density for the material powder was measured to be 0.61 ± 0.02 g cm^{-3} (standard deviation of 3 independent measurements), and the BET surface area was 2.9 m^2 g^{-1} (Fig. S3c).

3.4. Electrochemical evaluations of LMO, $Li_4Mn_5O_{12}$, LMNO

The voltage profile taken from the second cycle at each rate of the 3 materials paired with Li foil during rate capability cycling experiments is provided in Fig. 6. The discharge profile of LMO at C/20 had 2 distinct characteristic voltage plateaus at 4.1 V (two-phase reaction between λ-MnO_2 and $Li_{0.5}Mn_2O_4$) and at 4.0 V (single phase reaction between $Li_{0.5}Mn_2O_4$ and $LiMn_2O_4$) [69,70], reducing the averaged Mn oxidation state from 4+ back to 3.5+ [70]. The slow rate capacity reached more than 130 mAh g^{-1} LMO with first cycle coulombic efficiency of ~97%, and at 2C, the capacity still maintained ~95 mAh g^{-1} (Fig. 6a).

For $Li_4Mn_5O_{12}$, the single discharge voltage plateau at ~2.9 V was consistent with previous literature, suggesting that with partially substituted Mn by Li at 16c sites and increase in initial oxidation state of Mn (ideally 4+), the electrochemical activity shifted from 4 V down to ~3 V [71]. The first C/20 discharge reached over 150 mAh g^{-1} (out of theoretical 163 mAh g^{-1}) with coulombic efficiency of ~96% [72], and at 2C, ~85 mAh g^{-1} was retained (Fig. 6b). Both single Mn-based cathode materials exhibited good capacity and rate capability.

For multi-TM-based material LMNO with high compositional uniformity (Fig. 6c), at C/20, a very high fraction (>94%) of the discharge capacity was >4.5 V and there was a relatively small amount of capacity near ~4.1 V, indicating that most of the capacity resulted from Ni redox and not Mn redox [43,44]. The high amount of Ni redox and high voltage capacity indicated achieving the desired 3:1 Mn:Ni ratio in the active material and a high level of ordering of the Ni in the structure [73]. At C/2, the low capacity was attributed to (i) the upper cutoff voltage (4.9 V vs. Li/Li^+) was close to the operating voltage (4.7 V – 4.8 V) to prevent electrolyte decomposition (and thus the greater polarization at higher charge rates hit the cutoff voltage before extracting high fractions of the capacity) [74]; (ii) the high operating voltage resulted in more electrolyte degradation and thicker solid-electrolyte interphase formation relative to LMO and $Li_4Mn_5O_{12}$, which likely contributed to the relatively lower initial coulombic efficiency compared to the other electrode materials in this report of 84% [5]; and (iii) the high degree of cation ordering in the material may have lowered the relative rate capability [73].

CV profiles at four different scan rates for each material can be found in Fig. 7. For LMO and $Li_4Mn_5O_{12}$, the peaks in the CV profiles were consistent with the voltages where plateaus were observed during galvanostatic charge/discharge of the same materials (Fig. 6). For LMNO, only one reduction peak was observed in CV, which was attributed to the relatively fast scan rate and the small voltage interval between the two voltages associated with the $Ni^{2+/3+}$ and $Ni^{3+/4+}$ redox couples [75]. A dQ/dV plot calculated from the second charge/discharge cycle for LMNO at C/20 can be found in Supporting Information, Fig. S8. Two distinctive peaks were observed, as well as a small lower voltage peak attributed to a small amount of Mn^{3+} redox capacity. Thus, the individual redox processes being observed in dQ/dV suggested the lack of distinguishing them in CV may have been due to the scan rate applied. The peak current densities versus square root of scan rates were plotted (these can be found in Supporting Information, Fig. S9) to estimate the solid state diffusivity of Li^+ for each material [76,77]. LMO, $Li_4Mn_5O_{12}$, and LMNO were calculated using the slope of these fitted plots to be 4.4×10^{-11} cm^2 s^{-1}, 2.9×10^{-11} cm^2 s^{-1}, and 3.9×10^{-11} cm^2 s^{-1}, which were in the range of values previously reported in the literature [78–82]. The peak current densities versus scan rates were plotted (Fig. S10) to provide insights into the relevant electrochemical processes (either capacitive with slope of 1 or Faradaic with slope of 0.5) [76,77]. The slopes for LMO, $Li_4Mn_5O_{12}$, and LMNO were 0.65, 0.51, and 0.56, which would suggest primarily faradic reactions.

Cycle life tests with lithium foil anode were conducted at both C/5 and 2C rate, with the same rate applied for both charge and discharge. These results can be found in Supporting Information, Fig. S11 and S12, although LMNO at 2C has not been provided because its capacity was so low at that rate. For LMO, at C/5, the capacity at the 50th discharge was ~119 mAh g^{-1}, ~96% of the peak capacity in the cycle life test; at 2C, the capacity at the 500th discharge was ~84 mAh g^{-1}, ~75% of the peak capacity in the cycle life test. For $Li_4Mn_5O_{12}$, at C/5, the capacity at the 50th discharge was ~111 mAh g^{-1}, ~73% of the peak capacity in the cycle life test; at 2C, the capacity at the 500th

discharge was ~63 mAh g^{-1}, ~59% of the peak capacity in the cycle life test. For LMNO, at C/5, the capacity at the 50th discharge was ~116 mAh g^{-1}, ~93% of the peak capacity in the cycle life test. These results suggest good cycle life for the LMO at both rates, and also for the LMNO at relatively low rates of charge/discharge.

4. Conclusions

Herein was reported a route towards the synthesis of anisotropic Li-ion battery active material particles. These particle morphologies were desired as the first step needed for producing anisotropic particle assemblies towards potentially processing into anisotropic microstructures. The particles were produced from precursor materials synthesized using coprecipitation reactions in the presence of inhibitors. Evidence was provided that the addition of the inhibitor facilitated a transition of the precipitate to an anisotropic platelet morphology for all materials synthesized. In addition, for a multicomponent blend solution of Ni and Mn, evidence was provided that there was the development of a gradient in the composition of the transition metals deposited to form the particles, in particular in the radial direction. While gradient precursor particles have been previously reported, typically such gradients are achieved via control of the feed composition and not through differences in rates of deposition of transition metals. In this particular report, a gradient in composition was not desired, and thus high temperature annealing was used to facilitate relaxation of the compositional gradient for the multicomponent transition metal material. The precipitation synthesis for the precursors is scalable and translatable to multiple transition metal compositions, and thus it is expected that the methods reported can be used to produce a variety of compositions of cathode transition metal oxide active materials with anisotropic morphologies. Attention must be paid, however, when using such inhibitor to achieve anisotropic precursor morphologies because the coprecipitation reaction rate will likely be reduced and the transition metals do not necessarily deposit at the ratio of the feed when more than one transition metal is desired.

Declaration of Competing Interest

The authors declare that they have no known competing financial interests or personal relationships that could have appeared to influence the work reported in this paper.

Acknowledgements

This research was funded through support provided by a grant from the National Science Foundation, award CBET-1652488.

Appendix A. Supplementary data

Supplementary data to this article can be found online at https://doi.org/10.1016/j.powtec.2021.08.060.

References

[1] J.M. Tarascon, M. Armand, Issues and challenges facing rechargeable lithium batteries, Nature. 414 (2001) 359–367, https://doi.org/10.1038/35104644.
[2] J.B. Goodenough, Y. Kim, Challenges for rechargeable Li batteries, Chem. Mater. 22 (2010) 587–603, https://doi.org/10.1021/cm901452z.
[3] J.B. Goodenough, K.S. Park, The Li-ion rechargeable battery: a perspective, J. Am. Chem. Soc. 135 (2013) 1167–1176, https://doi.org/10.1021/ja3091438.
[4] K.M. Abraham, Prospects and limits of energy storage in batteries, J. Phys. Chem. Lett. 6 (2015) 830–844, https://doi.org/10.1021/jz5026273.
[5] Y. Di Zhang, Y. Li, X.H. Xia, X.L. Wang, C.D. Gu, J.P. Tu, High-energy cathode materials for Li-ion batteries: a review of recent developments, Sci. China Technol. Sci. 58 (2015) 1809–1828, https://doi.org/10.1007/s11431-015-5933-x.
[6] A. Kraytsberg, Y. Ein-Eli, A. Kraytsberg, Y. Ein-Eli, Higher, stronger, better ... A review of 5 volt cathode materials for advanced lithium-ion batteries, Adv. Energy Mater. 2 (2012) 922–939, https://doi.org/10.1002/aenm.201200068.
[7] S.B. Chikkannanavar, D.M. Bernardi, L. Liu, A review of blended cathode materials for use in Li-ion batteries, J. Power Sources 248 (2014) 91–100, https://doi.org/10.1016/j.jpowsour.2013.09.052.
[8] J.B. Goodenough, Cathode materials: a personal perspective, J. Power Sources 174 (2007) 996–1000, https://doi.org/10.1016/j.jpowsour.2007.06.217.
[9] S. Hwang, W. Chang, S.M. Kim, D. Su, D.H. Kim, J.Y. Lee, K.Y. Chung, E.A. Stach, Investigation of changes in the surface structure of LixNi 0.8Co0.15Al0.05O2 cathode materials induced by the initial charge, Chem. Mater. 26 (2014) 1084–1092, https://doi.org/10.1021/cm403332s.
[10] R.E. García, Y.-M. Chiang, W. Craig Carter, P. Limthongkul, C.M. Bishop, Microstructural modeling and design of rechargeable lithium-ion batteries, J. Electrochem. Soc. 152 (2005) A255, https://doi.org/10.1149/1.1836132.
[11] Z. Nie, R. Parai, C. Cai, C. Michaelis, J.M. LaManna, D. Hussey, D. Jacobson, D. Ghosh, G. Koenig, Pore microstructure impacts on lithium ion transport and rate capability of thick sintered electrodes, J. Electrochem. Soc. (2021) https://doi.org/10.1149/1945-7111/ac0bf6.
[12] Z. Nie, R. Parai, C. Cai, D. Ghosh, G. Koenig, Improving high rate cycling limitations of thick sintered battery electrodes by mitigating molecular transport limitations through modifying electrode microstructure and electrolyte conductivity, Mol. Syst. Des. Eng. (2021) https://doi.org/10.1039/d1me00082a.
[13] Z. Nie, S. Ong, D.S. Hussey, J.M. Lamanna, D.L. Jacobson, G.M. Koenig, Probing transport limitations in thick sintered battery electrodes with neutron imaging, Mol. Syst. Des. Eng. 5 (2020) 245–256, https://doi.org/10.1039/c9me00084d.
[14] C. Cai, Z. Nie, J.P. Robinson, D.S. Hussey, J.M. LaManna, D.L. Jacobson, G.M. Koenig, Thick sintered electrode lithium-ion battery discharge simulations: incorporating lithiation-dependent electronic conductivity and lithiation gradient due to charge cycle, J. Electrochem. Soc. 167 (2020) 140542, https://doi.org/10.1149/1945-7111/abc747.
[15] M. Ebner, D.W. Chung, R.E. García, V. Wood, Tortuosity anisotropy in lithium-ion battery electrodes, Adv. Energy Mater. 4 (2014) 1–6, https://doi.org/10.1002/aenm.201301278.
[16] J. Billaud, F. Bouville, T. Magrini, C. Villevieille, A.R. Studart, Magnetically aligned graphite electrodes for high-rate performance Li-ion batteries, Nat. Energy 1 (2016) 1–6, https://doi.org/10.1038/nenergy.2016.97.
[17] K. Du, L.H. Zhang, Y.B. Cao, Z.D. Peng, G.R. Hu, Synthesis of LiMn 0.8Fe 0.2PO 4/C by co-precipitation method and its electrochemical performances as a cathode material for lithium-ion batteries, Mater. Chem. Phys. 136 (2012) 925–929, https://doi.org/10.1016/j.matchemphys.2012.08.021.
[18] T. Ahmad, A. Ganguly, J. Ahmed, A.K. Ganguli, O.A.A. Alhartomy, Nanorods of transition metal oxalates: a versatile route to the oxide nanoparticles, Arab. J. Chem. 4 (2011) 125–134, https://doi.org/10.1016/j.arabjc.2010.06.041.
[19] Z. Yang, J. Lu, D. Bian, W. Zhang, X. Yang, J. Xia, G. Chen, H. Gu, G. Ma, Stepwise co-precipitation to synthesize LiNi1/3Co1/3Mn1/3O2one-dimensional hierarchical structure for lithium ion batteries, J. Power Sources 272 (2014) 144–151, https://doi.org/10.1016/j.jpowsour.2014.08.052.
[20] L. Zhang, W. Borong, L. Ning, W. Feng, Hierarchically porous micro-rod lithium-rich cathode material Li 1.2Ni0.13Mn0.54Co0.13O2 for high performance lithium-ion batteries, Electrochim. Acta 118 (2014) 67–74, https://doi.org/10.1016/j.electacta.2013.11.186.
[21] H. Dong, G.M. Koenig, A review on synthesis and engineering of crystal precursors produced: via coprecipitation for multicomponent lithium-ion battery cathode materials, CrystEngComm. 22 (2020) 1514–1530, https://doi.org/10.1039/c9ce00679f.
[22] L. Wang, D. Chen, J. Wang, G. Liu, W. Wu, G. Liang, Synthesis of LiNi0.5Mn1.5O4 cathode material with improved electrochemical performances through a modified solid-state method, Powder Technol. 292 (2016) 203–209, https://doi.org/10.1016/j.powtec.2016.02.002.
[23] R. Thirunakaran, G.H. Lew, W.-S. Yoon, Cerotic acid assisted sol-gel synthesis and electrochemical performance of double doped spinels (LiCrxMgyMn2-x-yO4) as cathode materials for lithium rechargeable batteries, Powder Technol. 301 (2016) 197–210, https://doi.org/10.1016/j.powtec.2016.05.064.
[24] I. Taniguchi, N. Fukuda, M. Konarova, Synthesis of spherical LiMn2O4 microparticles by a combination of spray pyrolysis and drying method, Powder Technol. 181 (2008) 228–236, https://doi.org/10.1016/j.powtec.2007.05.011.
[25] C. Belhomme, M. Cassir, J. Devynck, G. Gregoire, Synthesis by a soft chemistry route and characterization of LixNi1-xO ($0 < x < 0.5$) compounds: behavior in molten carbonates, J. Mater. Sci. 35 (2000) 2683–2688, https://doi.org/10.1023/A:1004793607621.
[26] M.E. Spahr, P. Novák, B. Schnyder, O. Haas, R. Nesper, Characterization of layered lithium nickel manganese oxides synthesized by a novel oxidative coprecipitation method and their electrochemical performance as lithium insertion electrode materials, J. Electrochem. Soc. 145 (1998) 1113–1121, https://doi.org/10.1149/1.1838425.
[27] H. Dong, A. Wang, G.M. Koenig, Role of coprecipitation and calcination of precursors on phase homogeneity and electrochemical properties of battery active materials, Powder Technol. 335 (2018) 137–146, https://doi.org/10.1016/j.powtec.2018.05.020.
[28] J.P. Robinson, G.M. Koenig, Tuning solution chemistry for morphology control of lithium-ion battery precursor particles, Powder Technol. 284 (2015) 225–230, https://doi.org/10.1016/j.powtec.2015.06.070.

[29] D. Liu, J. Han, J.B. Goodenough, Structure, morphology, and cathode performance of Li1-x[Ni0.5Mn1.5]O4 prepared by coprecipitation with oxalic acid, J. Power Sources 195 (2010) 2918–2923, https://doi.org/10.1016/j.jpowsour.2009.11.024.
[30] D. Wang, I. Belharouak, G. Zhou, K. Amine, Synthesis of lithium and manganese-rich cathode materials via an oxalate co-precipitation method, J. Electrochem. Soc. 160 (2013) A3108–A3112, https://doi.org/10.1149/2.016305jes.
[31] Z. Gao, S. Hu, X. Pan, L. Liu, S. Xie, C. Xie, H. Yuan, Controllable fabrication of Li-rich layered oxide Li1.2Mn0.54Ni0.13Co0.13O2 microspheres for enhanced electrochemical performance, CrystEngComm. 23 (2021) 4975–4984, https://doi.org/10.1039/d1ce00509j.
[32] X. Yao, Z. Xu, Z. Yao, W. Cheng, H. Gao, Q. Zhao, J. Li, A. Zhou, Oxalate co-precipitation synthesis of LiNi 0.6 Co 0.2 Mn 0.2 O 2 for low-cost and high-energy lithium-ion batteries, Mater. Today Commun. 19 (2019) 262–270, https://doi.org/10.1016/j.mtcomm.2019.02.001.
[33] Z. Qi, G.M. Koenig, High-performance LiCoO2 sub-micrometer materials from scalable microparticle template processing, ChemistrySelect. 1 (2016) 3992–3999, https://doi.org/10.1002/slct.201600872.
[34] Q. Liu, H. Zhu, J. Liu, X. Liao, Z. Tang, C. Zhou, M. Yuan, J. Duan, L. Li, Z. Chen, High-performance lithium-rich layered oxide material: effects of preparation methods on microstructure and electrochemical properties, Materials (Basel). 13 (2020) https://doi.org/10.3390/ma13020334.
[35] N. Wu, H. Wu, W. Yuan, S. Liu, J. Liao, Y. Zhang, Facile synthesis of one-dimensional LiNi0.8Co0.15Al0.05O2 microrods as advanced cathode materials for lithium ion batteries, J. Mater. Chem. A 3 (2015) 13648–13652, https://doi.org/10.1039/c5ta02767e.
[36] T.H. Cho, Y. Shiosaki, H. Noguchi, Preparation and characterization of layered LiMn1/3Ni1/3Co1/3O2 as a cathode material by an oxalate co-precipitation method, J. Power Sources 159 (2006) 1322–1327, https://doi.org/10.1016/j.jpowsour.2005.11.080.
[37] A. Angermann, J. Töpfer, Synthesis of nanocrystalline Mn-Zn ferrite powders through thermolysis of mixed oxalates, Ceram. Int. 37 (2011) 995–1002, https://doi.org/10.1016/j.ceramint.2010.11.019.
[38] U. García-Couceiro, O. Castillo, A. Luque, G. Beobide, P. Román, A new hydrated phase of cobalt(II) oxalate: crystal structure, thermal behavior and magnetic properties of {[Co(μ-ox)(H2O)2] · 2H2O}n, Inorg. Chim. Acta 357 (2004) 339–344, https://doi.org/10.1016/S0020-1693(03)00434-1.
[39] M.C. López, J.L. Tirado, C. Pérez Vicente, Structural and comparative electrochemical study of M(II) oxalates, M = Mn, Fe, Co, Ni, Cu, Zn, J. Power Sources 227 (2013) 65–71, https://doi.org/10.1016/j.jpowsour.2012.08.100.
[40] S. Guillemet-Fritsch, M. Aoun-Habbache, J. Sarrias, A. Rousset, N. Jongen, M. Donnet, P. Bowen, J. Lemaître, High-quality nickel manganese oxalate powders synthesized in a new segmented flow tubular reactor, Solid State Ionics 171 (2004) 135–140, https://doi.org/10.1016/S0167-2738(03)00282-0.
[41] M.M. Thackeray, W.I.F. David, P.G. Bruce, J.B. Goodenough, Lithium insertion into manganese spinels, Mater. Res. Bull. 18 (1983) 461–472, https://doi.org/10.1016/0025-5408(83)90138-1.
[42] T. Takada, H. Hayakawa, E. Akiba, Preparation and crystal structure refinement of Li4Mn5O12 by the rietveld method, J. Solid State Chem. 115 (1995) 420–426, https://doi.org/10.1006/jssc.1995.1154.
[43] R. Santhanam, B. Rambabu, Research progress in high voltage spinel LiNi0.5Mn1.5O4 material, J. Power Sources 195 (2010) 5442–5451, https://doi.org/10.1016/j.jpowsour.2010.03.067.
[44] H. Dong, G.M. Koenig, Compositional control of precipitate precursors for lithium-ion battery active materials: role of solution equilibrium and precipitation rate, J. Mater. Chem. A 5 (2017) 13785–13798, https://doi.org/10.1039/c7ta03653a.
[45] H. Dong, E. Gardner, A.F. Barron, G.M. Koenig, Apparent activation energy of multi-component transition metal oxalates to probe synthesis of battery precursor materials, Powder Technol. 354 (2019) 158–164, https://doi.org/10.1016/j.powtec.2019.05.082.
[46] S. Farmanesh, S. Ramamoorthy, J. Chung, J.R. Asplin, P. Karande, J.D. Rimer, Specificity of growth inhibitors and their cooperative effects in calcium oxalate monohydrate crystallization, J. Am. Chem. Soc. 136 (2014) 367–376, https://doi.org/10.1021/ja410623q.
[47] J. Chung, I. Granja, M.G. Taylor, G. Mpourmpakis, J.R. Asplin, J.D. Rimer, Molecular modifiers reveal a mechanism of pathological crystal growth inhibition, Nature. 536 (2016) 446–450, https://doi.org/10.1038/nature19062.
[48] S. Farmanesh, J. Chung, D. Chandra, R.D. Sosa, P. Karande, J.D. Rimer, High-throughput platform for design and screening of peptides as inhibitors of calcium oxalate monohydrate crystallization, J. Cryst. Growth 373 (2013) 13–19, https://doi.org/10.1016/j.jcrysgro.2012.09.018.
[49] J.J. De Yoreo, S.R. Qiu, J.R. Hoyer, Molecular modulation of calcium oxalate crystallization, Am. J. Physiol. Ren. Physiol. 291 (2006) 1123–1131, https://doi.org/10.1152/ajprenal.00136.2006.
[50] S.R. Qiu, A. Wierzbicki, C.A. Orme, A.M. Cody, J.R. Hoyer, G.H. Nancollas, S. Zepeda, J.J. De Yoreo, Molecular modulation of calcium oxalate crystallization by osteopontin and citrate, Proc. Natl. Acad. Sci. U. S. A. 101 (2004) 1811–1815, https://doi.org/10.1073/pnas.0307900100.
[51] L. Wang, W. Zhang, S.R. Qiu, W.J. Zachowicz, X. Guan, R. Tang, J.R. Hoyer, J.J.D. Yoreo, G.H. Nancollas, Inhibition of calcium oxalate monohydrate crystallization by the combination of citrate and osteopontin, J. Cryst. Growth 291 (2006) 160–165, https://doi.org/10.1016/j.jcrysgro.2006.02.032.
[52] A.N. Puzan, V.N. Baumer, D.V. Lisovytskiy, P.V. Mateychenko, Structure disordering and thermal decomposition of manganese oxalate dihydrate, MnC2O4·2H2O, J. Solid State Chem. 260 (2018) 87–94, https://doi.org/10.1016/j.jssc.2018.01.022.
[53] A.N. Puzan, V.N. Baumer, D.V. Lisovytskiy, P.V. Mateychenko, Structure transformations in nickel oxalate dihydrate NiC2O4·2H2O and nickel formate dihydrate Ni(HCO2)2·2H2O during thermal decomposition, J. Solid State Chem. 266 (2018) 133–142, https://doi.org/10.1016/j.jssc.2018.07.005.
[54] N. Mancilla, V. Caliva, M.C. D'Antonio, A.C. González-Baró, E.J. Baran, Vibrational spectroscopic investigation of the hydrates of manganese(II) oxalate, J. Raman Spectrosc. 40 (2009) 915–920, https://doi.org/10.1002/jrs.2200.
[55] R. Deyrieux, C. Berro, A. Peneloux, Structure crystalline des oxalates dihydrates de manganèse, de cobalt, de nikel et de zinc, Bull. Soc. Chim. Fr. 1 (1973) 25–33.
[56] Y. Shimakawa, T. Numata, J. Tabuchi, Verwey-type transition and magnetic properties of the LiMn2O4Spinels, J. Solid State Chem. 131 (1997) 138–143, https://doi.org/10.1006/jssc.1997.7366.
[57] G. Yang, W. Yan, J. Wang, H. Yang, Fabrication and formation mechanism of Mn2O3 hollow nanofibers by single-spinneret electrospinning, CrystEngComm. 16 (2014) 6907–6913, https://doi.org/10.1039/c4ce00521j.
[58] M.L.P. Le, P. Strobel, C.V. Colin, T. Pagnier, F. Alloin, Spinel-type solid solutions involving Mn4+ and Ti 4+:crystal chemistry, magnetic and electrochemical properties, J. Phys. Chem. Solids 72 (2011) 124–135, https://doi.org/10.1016/j.jpcs.2010.11.010.
[59] R.D. Shannon, Revised effective ionic radii and systematic studies of interatomic distances in halides and chalcogenides, Acta Crystallogr. Sect. A Cryst. Physics, Diffraction, Theor. Gen. Crystallogr. 32 (1976) 751–767.
[60] G.M. Koenig, I. Belharouak, H. Deng, Y.K. Sun, K. Amine, Composition-tailored synthesis of gradient transition metal precursor particles for lithium-ion battery cathode materials, Chem. Mater. 23 (2011) 1954–1963, https://doi.org/10.1021/cm200058c.
[61] J.I. Goldstein, D.E. Newbury, J.R. Michael, N.W.M. Ritchie, J.H.J. Scott, D.C. Joy, Scanning electron Microscopy and X-Ray Microanalysis, Springer, 2017.
[62] Y.K. Sun, B.R. Lee, H.J. Noh, H. Wu, S.T. Myung, K. Amine, A novel concentration-gradient Li[Ni0.83Co0.07Mn 0.10]O2 cathode material for high-energy lithium-ion batteries, J. Mater. Chem. 21 (2011) 10108–10112, https://doi.org/10.1039/c0jm04242k.
[63] P. Hou, H. Zhang, Z. Zi, L. Zhang, X. Xu, Core-shell and concentration-gradient cathodes prepared via co-precipitation reaction for advanced lithium-ion batteries, J. Mater. Chem. A 5 (2017) 4254–4279, https://doi.org/10.1039/c6ta10297b.
[64] Y.K. Sun, S.T. Myung, B.C. Park, J. Prakash, I. Belharouak, K. Amine, High-energy cathode material for long-life and safe lithium batteries, Nat. Mater. 8 (2009) 320–324, https://doi.org/10.1038/nmat2418.
[65] A. Manthiram, K. Chemelewski, E.S. Lee, A perspective on the high-voltage LiMn1.5Ni0.5O 4 spinel cathode for lithium-ion batteries, Energy Environ. Sci. 7 (2014) 1339–1350, https://doi.org/10.1039/c3ee42981d.
[66] J. Song, D.W. Shin, Y. Lu, C.D. Amos, A. Manthiram, J.B. Goodenough, Role of oxygen vacancies on the performance of Li[Ni 0.5-xMn 1.5+ x]O 4 (x = 0, 0.05, and 0.08) spinel cathodes for lithium-ion batteries, Chem. Mater. 24 (2012) 3101–3109, https://doi.org/10.1021/cm301825h.
[67] L. Wan, Y. Deng, C. Yang, H. Xu, X. Qin, G. Chen, Ni/Mn ratio and morphology-dependent crystallographic facet structure and electrochemical properties of the high-voltage spinel LiNi0.5Mn1.5O4 cathode material, RSC Adv. 5 (2015) 25988–25997, https://doi.org/10.1039/c5ra03602j.
[68] D. Gryffroy, R.E. Vandenberghe, E. Legrand, A neutron diffraction study of some spinel compounds containing octahedral Ni and Mn at a 1:3 ratio, Mater. Sci. Forum 79–82 (1991) 785–790, https://doi.org/10.4028/www.scientific.net/MSF.79-82.785.
[69] H. Zhao, X. Liu, C. Cheng, Q. Li, Z. Zhang, Y. Wu, B. Chen, W. Xiong, Synthesis and electrochemical characterizations of spinel LiMn1.94MO4 (M = Mn0.06, Mg0.06, Si0.06, (Mg0.03Si0.03)) compounds as cathode materials for lithium-ion batteries, J. Power Sources 282 (2015) 118–128, https://doi.org/10.1016/j.jpowsour.2015.02.049.
[70] A.H. Marincaş, F. Goga, S.A. Dorneanu, P. Ilea, Review on synthesis methods to obtain LiMn2O4-based cathode materials for Li-ion batteries, J. Solid State Electrochem. 24 (2020) 473–497, https://doi.org/10.1007/s10008-019-04467-3.
[71] J. Kim, A. Manthiram, Low temperature synthesis and electrode properties of Li4Mn5 O 12, J. Electrochem. Soc. 145 (1998) L53–L55, https://doi.org/10.1149/1.1838412.
[72] C. Alié, C. Calberg, C. Páez, D. Liquet, D. Eskenazi, B. Heinrichs, N. Job, Electrochemical performances of Li4Mn5O12 films prepared by spray-coated sol-gel reaction, J. Power Sources 403 (2018) 173–183, https://doi.org/10.1016/j.jpowsour.2018.09.081.
[73] Z. Moorhead-Rosenberg, A. Huq, J.B. Goodenough, A. Manthiram, Electronic and electrochemical properties of Li1-xMn1.5Ni0.5O4 spinel cathodes as a function of lithium content and cation ordering, Chem. Mater. 27 (2015) 6934–6945, https://doi.org/10.1021/acs.chemmater.5b01356.
[74] D. Aurbach, Y. Talyosef, B. Markovsky, E. Markevich, E. Zinigrad, L. Asraf, J.S. Gnanaraj, H.J. Kim, Design of electrolyte solutions for Li and Li-ion batteries: a review, Electrochim. Acta 50 (2004) 247–254, https://doi.org/10.1016/j.electacta.2004.01.090.
[75] D.W. Shin, C.A. Bridges, A. Huq, M.P. Paranthaman, A. Manthiram, Role of cation ordering and surface segregation in high-voltage spinel LiMn LiMn 1.5Ni 0.5-xM xO 4 (M = Cr, Fe, and Ga) cathodes for lithium-ion batteries, Chem. Mater. 24 (2012) 3720–3731, https://doi.org/10.1021/cm301844w.
[76] T. Kim, W. Choi, H.C. Shin, J.Y. Choi, J.M. Kim, M.S. Park, W.S. Yoon, Applications of voltammetry in lithium ion battery research, J. Electrochem. Sci. Technol. 11 (2020) 14–25, https://doi.org/10.33961/jecst.2019.00619.

[77] H. Lindström, S. Södergren, A. Solbrand, H. Rensmo, J. Hjelm, A. Hagfeldt, S.E. Lindquist, Li+ ion insertion in TiO2 (anatase). 2. Voltammetry on nanoporous films, J. Phys. Chem. B 101 (1997) 7717–7722, https://doi.org/10.1021/jp970490q.
[78] H. Xia, Y.S. Meng, L. Lu, G. Ceder, Electrochemical properties of nonstoichiometric LiNi[sub 0.5]Mn[sub 1.5]O[sub 4−δ] thin-film electrodes prepared by pulsed laser deposition, J. Electrochem. Soc. 154 (2007) A737, https://doi.org/10.1149/1.2741157.
[79] Q. Wu, X. Zhang, S. Sun, N. Wan, D. Pan, Y. Bai, H. Zhu, Y.S. Hu, S. Dai, Improved electrochemical performance of spinel LiMn1.5Ni0.5O4 through MgF2 nano-coating, Nanoscale. 7 (2015) 15609–15617, https://doi.org/10.1039/c5nr03564c.
[80] B.T. Habte, F. Jiang, Microstructure reconstruction and impedance spectroscopy study of LiCoO2, LiMn2O4 and LiFePO4 Li-ion battery cathodes, Microporous Mesoporous Mater. 268 (2018) 69–76, https://doi.org/10.1016/j.micromeso.2018.04.001.
[81] Y.K. Sun, S.H. Jin, Synthesis and electrochemical characteristics of spinel phase LiMn2O4-based cathode materials for lithium polymer batteries, J. Mater. Chem. 8 (1998) 2399–2404, https://doi.org/10.1039/a804483j.
[82] A. Nagasubramanian, Studies of Manganese Based Oxides as Alternative Electrode Materials for Lithium Based Energy Storage Devices, 2016.